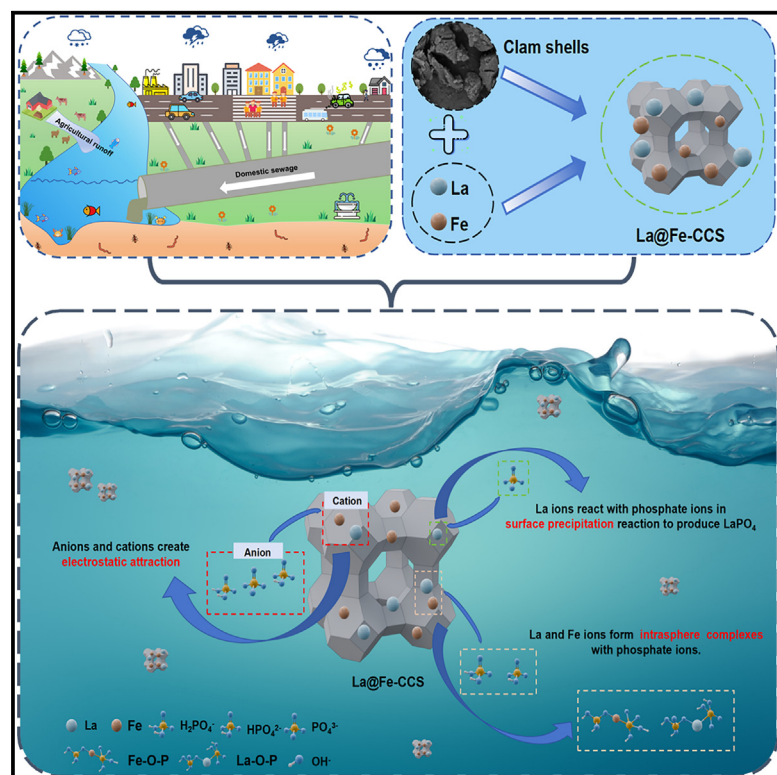# Recyclable adsorbents of Fe and La co-modified clam shells for phosphorus removal from domestic sewage: Characterization and mechanisms

Graphical abstract

Highlights

- Magnetic La/Fe co-modified clam shells were prepared using the precipitation method

- La@Fe-CCS showed fast kinetics (20 min) and high adsorption capacity (43.61 mg/g)

- La@Fe-CCS demonstrated excellent recyclability and regenerative properties

- La@Fe-CCS effectively removed TP from domestic sewage, with a removal rate over 95%

Authors

Huiteng Wang, Hui Luo, Teng Qin, ..., Ming Tang, Bao-Jie He, Zhaoqian Jing

Correspondence

water@njfu.edu.cn (H.L.),
baojie.he@cqu.edu.cn (B.-J.H.)

In brief

Chemistry; Chemical engineering

CellPress

iScience

Article

Recyclable adsorbents of Fe and La co-modified clam shells for phosphorus removal from domestic sewage: Characterization and mechanisms

Huiteng Wang,[1] Hui Luo,[1,2,5,*] Teng Qin,[1] Jing Yang,[1] Limin Chen,[1] Meng Liu,[1] Ming Tang,[1] Bao-Jie He,[3,*] and Zhaoqian Jing[4]

[1]School of Civil and Ocean Engineering, Jiangsu Ocean University, Lianyungang 222005, China
[2]Institute of Oceanology, Chinese Academy of Sciences, Qingdao 266071, China
[3]Centre for Climate–Resilient and Low–Carbon Cities, School of Architecture and Urban Planning, Key Laboratory of New Technology for Construction of Cities in Mountain Area, Ministry of Education, Chongqing University, Chongqing 400030, China
[4]College of Civil Engineering, Nanjing Forestry University, Nanjing 210037, China
[5]Lead contact
*Correspondence: water@njfu.edu.cn (H.L.), baojie@cqu.edu.cn (B.-J.H.)
https://doi.org/10.1016/j.isci.2025.111762

SUMMARY

This research focused on creating a recyclable magnetic adsorbent, termed La@Fe-CCS, which was modified with lanthanum (La) to improve its efficiency in removing phosphate. The process involved integrating lanthanum into an iron (Fe)-based clam shell matrix (Fe-CCS). This study showed that La@Fe-CCS demonstrated superior adsorption capabilities within a pH range of 3–8 compared to Fe-CCS. Coexisting ions and humic acid (HA) had limited effects. La@Fe-CCS also exhibited rapid adsorption kinetics, achieving equilibrium within 20 min. It showed a theoretical maximum adsorption capacity of 43.61 mg/g, which was substantially higher than that of Fe-CCS (5.79 mg/g). XPS and FTIR analyses indicated that phosphate removal by La@Fe-CCS involves ligand exchange between surface hydroxyl groups and phosphate, as well as intrasphere complexation. In real domestic sewage, La@Fe-CCS achieved over 95% total phosphorus (P) removal. These results suggest that La@Fe-CCS is a highly efficient adsorbent for practical P remediation applications.

INTRODUCTION

Clams, a common marine mollusk in China, are known for their taste, nutritional benefits, and medicinal properties. Clams can be cultivated under suitable artificial conditions,[1] making them one of the most important aquatic resources in China. However, with the development of the mariculture industry in China, clam production has grown exponentially, and its by-product, clam shells (CS), accounted for approximately 16% of global production as of 2020, causing substantial environmental pollution.[2] This is because CS are predominantly composed of 95–99% calcium carbonate ($CaCO_3$), which is resistant to degradation by microorganisms and requires a significant amount of time to decompose in the natural environment, leading to substantial accumulation of CS on soil surfaces or their flotation on water for extended periods.[3] Consequently, the flesh and other organic matter retained within the CS remain exposed to the environment for prolonged durations. This produces unpleasant odors and leads to microbial decay and decomposition, releasing toxic gases, such as carbon disulfide (CS_2) and ammonia (NH_3), which pose serious risks to human health.[4]

Consequently, the innovative and sustainable recycling of CS to turn this waste into valuable materials is critical. CS has been explored for several applications, such as bio-oil catalysts, organic dye photodegradation, constituents of flame-retardant coatings,[5–7] water treatment for heavy metal removal,[8] and phosphorus (P) fertilizer synthesis.[9] Recently, the potential of CS for P removal from water has attracted growing interest, as excessive P leads to eutrophication,[10] resulting in cyanobacterial blooms and the degradation of water quality.[11] Therefore, controlling external P inputs has become an urgent need to maintain the health and ecological balance of aquatic environments. The main external sources of P include agricultural activities, municipal sewage, and industrial wastewater. Previous studies have shown that total P (TP) concentrations entering freshwater systems and other confined water bodies should not exceed 0.05 mg/L.[12] As a result, many municipal sewage treatment plants commonly implement control measures for P. The adsorption technique, recognized for its affordability and ease of use, has been extensively used in P removal processes.

Nguyen et al.[13] prepared WHC-M800 by calcining CS, increasing its ability to adsorb phosphate to 38.7 mg/g. Souza et al.[14] thoroughly mixed the CS with sludge and then calcined them to produce ADSX, which demonstrated a phosphate adsorption capacity of 21.359 mg/g. Khan et al.[15] modified the calcined CS with sodium hydroxide and hydrochloric acid, which

yielded a phosphate adsorption capacity of 77.23 mg/g. The modification methods mentioned above have enhanced the phosphate adsorption capacity of CS to varying degrees. Unfortunately, the modified CS mentioned above exhibited excellent adsorption properties only in the high pH range (9–11), limiting their application scenarios (for example, domestic sewage typically has a pH around 7). Additionally, the adsorption time ranged from 4.5 to 24 h, further reducing their usefulness. Recently, in the study of other bivalve shells, Yin et al.[16] prepared three metal-TMS composites. Although these composites maintained good adsorption properties in a relatively low pH range (6–9), none of them were magnetic, complicating recycling and reuse efforts. This is clearly not aligned with the current concept of sustainable green development.

In this sense, magnetic adsorbents, particularly La-based materials, have shown promise due to their enhanced adsorption capability, broader pH application range, and recyclability. La is an environmentally friendly and abundantly available rare earth element that can be incorporated into materials to enhance dispersion and serve as active sites, thereby improving their ability to adsorb phosphate.[17] When La-based adsorbents are combined with Fe, they can be magnetically recycled, mitigating secondary pollution. Irfan et al.[18] demonstrated that Fe/La co-modified biochar (Fe-La@CBC) exhibits a significantly higher phosphate adsorption capacity of 10 mg/g compared to Fe-based (6.679 mg/g) biochar and pure La-based biochar (7.87 mg/g). Importantly, Fe-based adsorbents and pure La-based adsorbents have a higher risk of re-releasing P from their surfaces due to external environmental changes compared to magnetic La-based adsorbents.[19] Liu et al.[20] prepared magnetic La-based attapulgite (M-LaFeAP) with a saturated magnetization strength of 25.83 emu/g, allowing it to be effectively recovered from water and maintains excellent adsorption capacity (up to 43.34 mg/g) in the pH range of 2–10. In another study, Lan et al.[21] introduced La-Fe into chitosan beads to prepare nano LaFe@CS, which demonstrated that it gradually reached saturation adsorption in approximately 2 h. After magnetic recycling, it maintained a phosphate adsorption capacity of 78.5% after four adsorption cycles. These studies highlight the superiority of magnetic La-based adsorbents in phosphate removal.

The aforementioned literature indicates that the modified CS encountered difficulties in recycling and reuse, prolonged adsorption times, a narrow range of applicable pH values, and several other issues. Consequently, these issues limit the potential of CS for effective phosphate removal in real water bodies, posing challenges to its application prospects in the field of water treatment. In contrast, magnetic La-based adsorbents may address these issues. Based on this, the present study proposes the co-modification of CS with bimetallic (La/Fe) to develop a magnetic, recyclable La-based CS adsorbent (La@Fe-CCS). The adsorbent was expected to exhibit advantages, such as rapid adsorption, strong resistance to interference, and recyclability. The main objectives include (1) synthesizing La@Fe-CCS for phosphate removal from domestic sewage; (2) evaluating its adsorption performance and mechanisms; (3) assessing its pH tolerance and ion interference; and (4) examining its cyclic regeneration performance and effectiveness in removing phosphate in real sewage treatment scenarios. This research offers a novel, sustainable approach to mitigating eutrophication in water bodies and repurposing waste CS from aquaculture.

RESULTS AND DISCUSSION

Characterization of raw materials

SEM-EDS, X-ray diffraction (XRD), and Brunauer-Emmet-Teller (BET) analyses were performed on both CS and CCS, with the results shown in Figure 1. Figures 1A and 1C SEM results showed that the morphology of CCS changed after calcination. Specifically, there was an increase in crystals on the surface of CCS, which were hypothesized to be CaO, produced by the thermal decomposition of $CaCO_3$ in CS.[22] Figures 1B and 1D EDS results showed that CS was mainly composed of C, Ca, and O. After calcination, the Ca content in CCS increased. XRD patterns (Figures 1E and 1H) revealed that CS primarily consisted of $CaCO_3$ with trace amounts of SiO_2, while calcination introduced CaO peaks (2θ = 17.92°, 28.30°, 34.28°, 47.42°, 50.24°), which were consistent with the SEM analysis. Figures 1F, 1I, 1G, and 1J showed the N_2 adsorption-desorption isothermal curves and pore size distribution curves of CS and CCS, respectively. According to the IUPAC classification analysis,[23] both CS and CCS had type IV isothermal adsorption curves and exhibited adsorption hysteresis within the relative pressure P/P_0 range of 0.6–0.9, with the presence of H_3-type hysteresis loops, indicating that the two materials were porous structures. The pore diameters of CS and CCS were concentrated in the range of 2–50 nm, indicating that both materials were predominantly mesoporous. In addition, compared with CS (2.03–17.67 nm), the pore diameter distribution of CCS was primarily concentrated in the range of 2.77–35 nm, indicating that the mesoporous structure of CCS was more pronounced, which was highly favorable for the impregnation of active sites.

Characterization of Fe-CCS and La@Fe-CCS

The structural and compositional features of Fe-CCS and La@Fe-CCS were investigated using SEM-EDS, XRD, and BET analysis, with results presented in Figure 2. From Figure 2A, it is clear that Fe modification caused the smooth surface of CCS to become rougher, with visible crystal formations and an increased number of pores. The EDS results in Figure 2B further support this observation, showing a significant increase in Fe content on the surface of Fe-CCS (48.31%) compared to CCS (0.70%), reflecting Fe loading onto CCS. Upon La modification, numerous granular crystals were uniformly distributed across the surface of La@Fe-CCS, as seen in Figure 2C. Additionally, La@Fe-CCS exhibited a more prominent porous structure. The results indicated that La was likely successfully deposited onto the surface of the material in a granular form,[24] and further enhanced the pore structure of the material. The EDS results revealed a La content of 14.04% on the La@Fe-CCS surface (Figure 2D), confirming the successful incorporation of La. Notably, this research achieved higher La contents compared to prior studies, such as M-LaFeBT (12.77%) and LMZ (9.90%),[25,26] suggesting that La@Fe-CCS may offer superior adsorption performance.

Figures 2E and 2H reveal that the Fe-CCS XRD pattern displayed distinct peaks characteristic of magnetite (2θ = 30.22°,
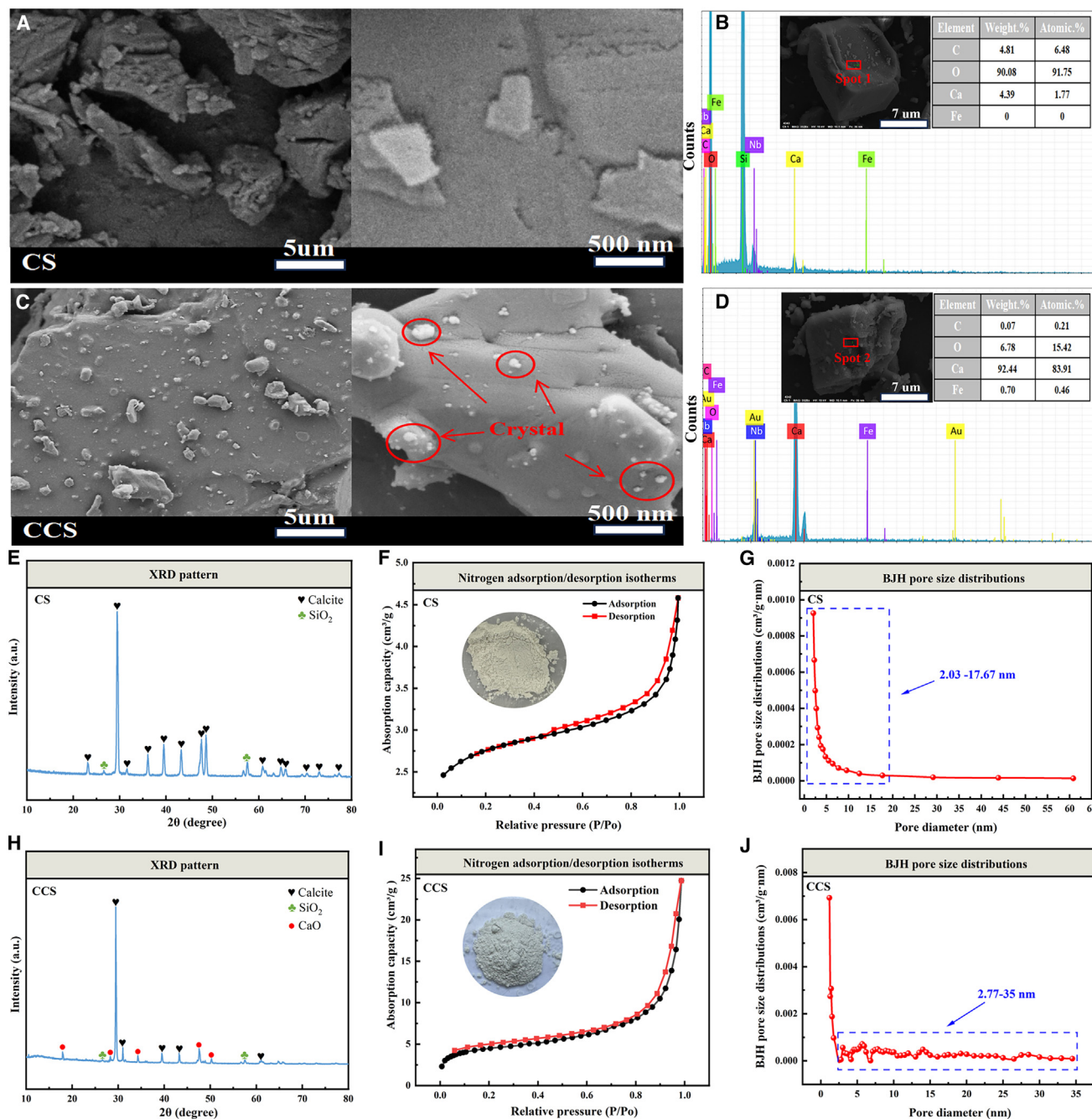
Figure 1. SEM images, EDS data, XRD patterns, N₂ adsorption-desorption isotherms, and BJH PSDs of the materials
(A, B, and E–G) CS.
(C, D, and H–J) CCS.

$35.60°$, $43.67°$, $53.31°$, $57.22°$, $62.84°$, $71.31°$, $74.36°$), confirming the presence of Fe_3O_4. The XRD spectrum of La@Fe-CCS revealed not only the characteristic peaks of magnetite but also those belonging to the hexagonal phase of lanthanum hydroxide ($2\theta = 24.30°$, $29.06°$, $75.16°$). This indicated that lanthanum hydroxide had formed in La@Fe-CCS after La modification. The results of the N_2 adsorption-desorption isothermal curves in

Figures 2F and 2I showed that the isothermal adsorption curves of Fe-CCS and La@Fe-CCS still belonged to the H_3 hysteresis line in type IV after Fe or Fe/La modification, and the adsorption and desorption isotherms for the two materials did not overlap completely. Combined with the results of the BJH pore size distribution curves (Figures 2G and 2J), the pore diameters of both materials were distributed within 5–36 nm, which indicated that
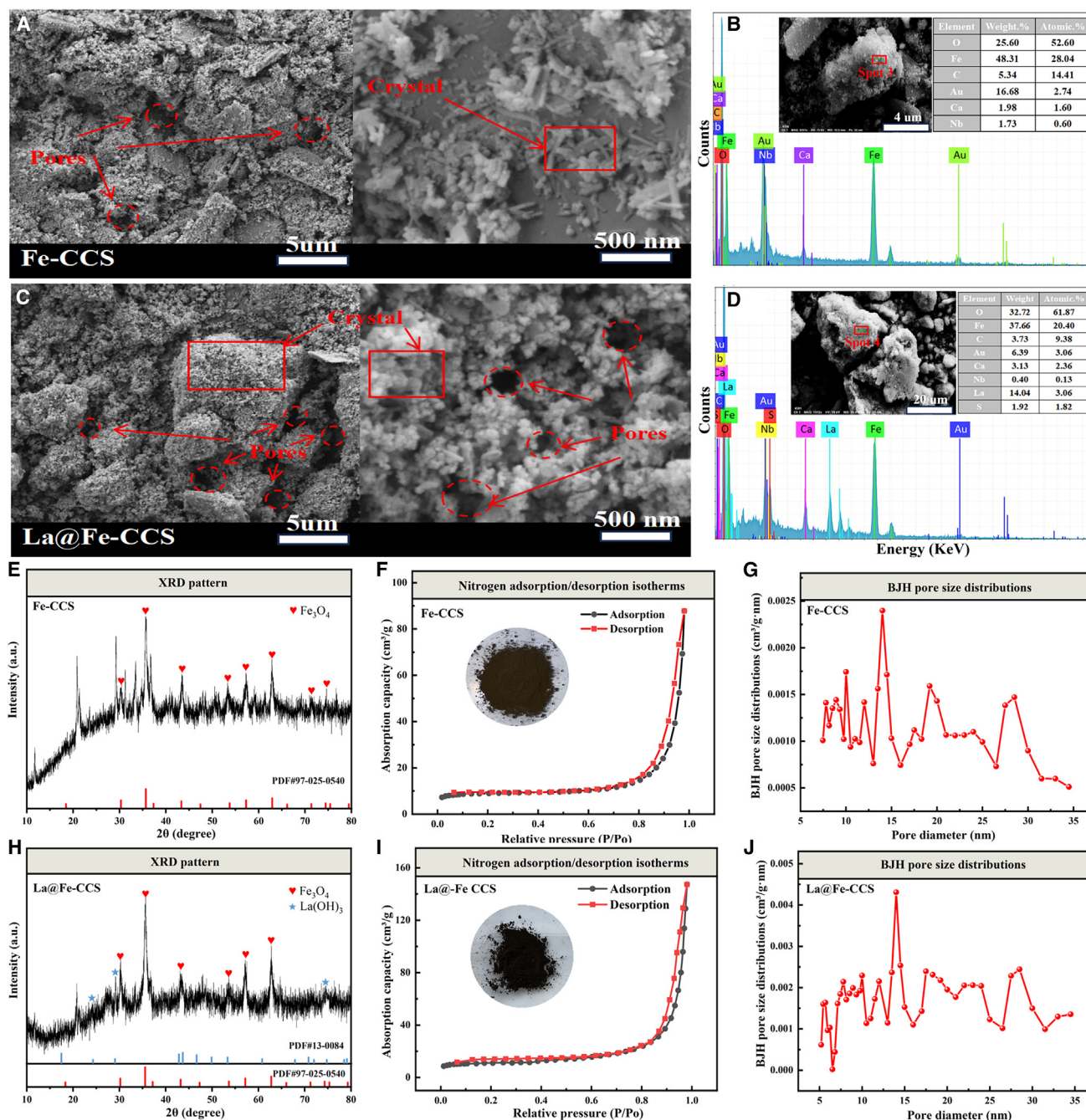
Figure 2. SEM images, EDS data, XRD patterns, N₂ adsorption-desorption isotherms, and BJH PSDs of the materials
(A, B, and E–G) Fe-CCS.
(C, D, and H–J) La@Fe-CCS.

both materials retained their porous structure after modification and were mainly composed of mesopores.

The BET surface area results for CS, CCS, Fe-CCS, and La@Fe-CCS (Table 1) indicate that calcination of CS increased its specific surface area (SSA) to 4.57 m²/g by removing impurities from the pores. Following Fe modification, SSA, pore volume, and average pore diameter of Fe-CCS increased to 30.35 m²/g, 0.093 cm³/g, and 26.09 nm, respectively, indicating that Fe modification effectively improved the SSA and pore structure. Notably, La modification further increased the SSA of La@Fe-CCS to 37.42 m²/g, 8.89 times that of CS, providing more active sites for phosphate adsorption. The pore volume of La@Fe-CCS (0.185 cm³/g) was also significantly higher than that of CS (0.023 cm³/g). This may be caused by Fe and La

Table 1. Structural parameters of selected materials

Composition	BET surface area (m^2/g)	Pore volume (cm^3/g)	Average pore size (nm)
CS	4.21	0.023	20.64
CCS	4.57	0.018	13.85
Fe-CCS	30.35	0.093	26.09
La@Fe-CCS	37.42	0.185	24.34

loading onto the surface of CS, followed by agglomeration. The average pore diameter of La@Fe-CCS increased to 24.34 nm after modification, which helped improve adsorption capacity.[24]
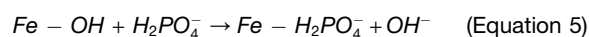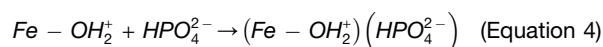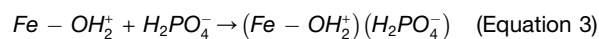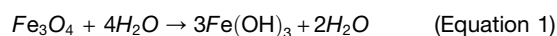
Magnetic properties are critical for assessing the recoverability of magnetic adsorbents. The vibrating sample magnetometeric (VSM) results (Figure 3A) revealed that the saturation magnetization values for Fe-CCS and La@Fe-CCS were 16.51 emμ/g and 14.12 emμ/g, respectively. Although the saturation magnetization of La@Fe-CCS was slightly lower than that of Fe-CCS due to the addition of La, it still exhibited sufficient magnetic properties for recovery. As demonstrated in the inset of Figure 3A, both materials could be effectively recovered using an external magnetic field, as indicated by the clear water without suspended particles, ensuring their feasibility for subsequent phosphate recovery applications.

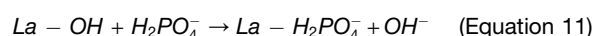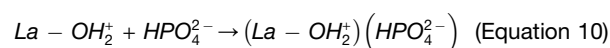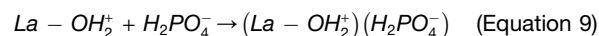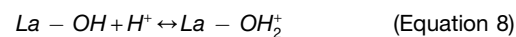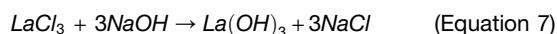### Impacts of pH, coexisting ions, and humic acid
Studies show that pH is a crucial parameter affecting adsorption by adsorbents, directly influencing the ionic form of phosphate and its chemical behavior in solution. Figure 3B shows the distribution of phosphate species at various pH levels. At pH < 2.15, H_3PO_4 is the predominant species, while $H_2PO_4^-$ dominates between pH 2.15 and 7.20, HPO_4^{2-} between pH 7.20 to 12.31, and PO_4^{3-} at pH > 12.31. The pH impact on phosphate adsorption by Fe-CCS and La@Fe-CCS is illustrated in Figures 3C and 3D. Both adsorbents exhibited a trend of increasing adsorption capacity with pH, followed by a decline, indicating that adsorption is highly pH-dependent.

Phosphate adsorption on Fe-based adsorbents is usually thought to occur through electrostatic interactions or ligand exchange between the phosphate anion and the $Fe-OH_2^+$ sites, where phosphate oxygen replaces surface hydroxyl oxygen.[18] Specifically, at pH 2, the H_3PO_4 predominates in the solution, resulting in weak electrostatic attraction and low adsorption due to the lack of ion exchange with Fe-CCS. As the pH increased to between 3 and 6, the adsorption capacity of Fe-CCS improved and stabilized, likely due to the hydroxylation of magnetite (Equation 1), forming Fe-OH groups on the surface which are protonated under acidic conditions (Equation 2). In this range, $H_2PO_4^-$ is the dominant species, together with a minimal contribution of HPO_4^{2-}, and their interaction with $Fe-OH_2^+$ (Equations 3 and 4) enhances adsorption through electrostatic attraction and ligand exchange (Equation 5). As the pH continued to increase, the rising concentration of OH^- ions competes with phosphate anions for available adsorption sites, thereby reducing the adsorption capacity of Fe-CCS. Electrostatic repulsion and limited ligand exchange (Equation 6) also contributed to a significantly reduced adsorption capacity. Overall, Fe-CCS

maintained a high adsorption capacity within the pH range of 3–6.

$$Fe_3O_4 + 4H_2O \rightarrow 3Fe(OH)_3 + 2H_2O \quad \text{(Equation 1)}$$

$$Fe - OH + H^+ \leftrightarrow Fe - OH_2^+ \quad \text{(Equation 2)}$$

$$Fe - OH_2^+ + H_2PO_4^- \rightarrow (Fe - OH_2^+)(H_2PO_4^-) \quad \text{(Equation 3)}$$

$$Fe - OH_2^+ + HPO_4^{2-} \rightarrow (Fe - OH_2^+)(HPO_4^{2-}) \quad \text{(Equation 4)}$$

$$Fe - OH + H_2PO_4^- \rightarrow Fe - H_2PO_4 + OH^- \quad \text{(Equation 5)}$$

$$Fe \equiv OH + HPO_4^{2-} \rightarrow (FeHPO_4)^+ + 3OH^- \quad \text{(Equation 6)}$$

Compared to Fe-CCS, La@Fe-CCS demonstrated superior phosphate adsorption, maintaining over 90% phosphate removal efficiency within a pH range of 3–8. This was likely due to the fact that main adsorption site for phosphate in La@Fe-CCS was La. Briefly, La@Fe-CCS was modified with NaOH, which converted $LaCl_3$ to $La(OH)_3$ (Equation 7), forming La-OH groups on the surface of La@Fe-CCS. These groups became protonated under acidic conditions (Equation 8), allowing for efficient phosphate removal via electrostatic attraction (Equations 9 and 10) and ligand exchange (Equation 11). However, as the pH increased above 8, the affinity for divalent HPO_4^{2-} decreased, leading to a reduction in adsorption capacity. As the pH continued to increase, electrostatic repulsion between OH^- and HPO_4^{2-} hindered phosphate adsorption (Equation 12). Therefore, the main mechanisms for phosphate removal by Fe-CCS and La@Fe-CCS were hypothesized to involve both nonspecific electrostatic interactions and specific ligand exchange.

$$LaCl_3 + 3NaOH \rightarrow La(OH)_3 + 3NaCl \quad \text{(Equation 7)}$$

$$La - OH + H^+ \leftrightarrow La - OH_2^+ \quad \text{(Equation 8)}$$

$$La - OH_2^+ + H_2PO_4^- \rightarrow (La - OH_2^+)(H_2PO_4^-) \quad \text{(Equation 9)}$$

$$La - OH_2^+ + HPO_4^{2-} \rightarrow (La - OH_2^+)(HPO_4^{2-}) \quad \text{(Equation 10)}$$

$$La - OH + H_2PO_4^- \rightarrow La - H_2PO_4 + OH^- \quad \text{(Equation 11)}$$

$$La \equiv OH + HPO_4^{2-} \rightarrow (LaHPO_4)^+ + 3OH^- \quad \text{(Equation 12)}$$

Besides having rapid and high adsorption capacity, effective adsorbents must also withstand interference from coexisting ions in practical applications, as sewage typically contains various competing ions. Figure 3E illustrates the impact of common ions on phosphate adsorption, indicating that at low concentrations, coexisting ions had a minimal effect on the adsorption performance of Fe-CCS and La@Fe-CCS. However, at an anion concentration of 100 mg/L, SO_4^{2-}, Cl^-, and NO_3^- had little impact, whereas CO_3^{2-} significantly reduced the adsorption capacity of both adsorbents, by 59.69% for Fe-CCS and 35.61%
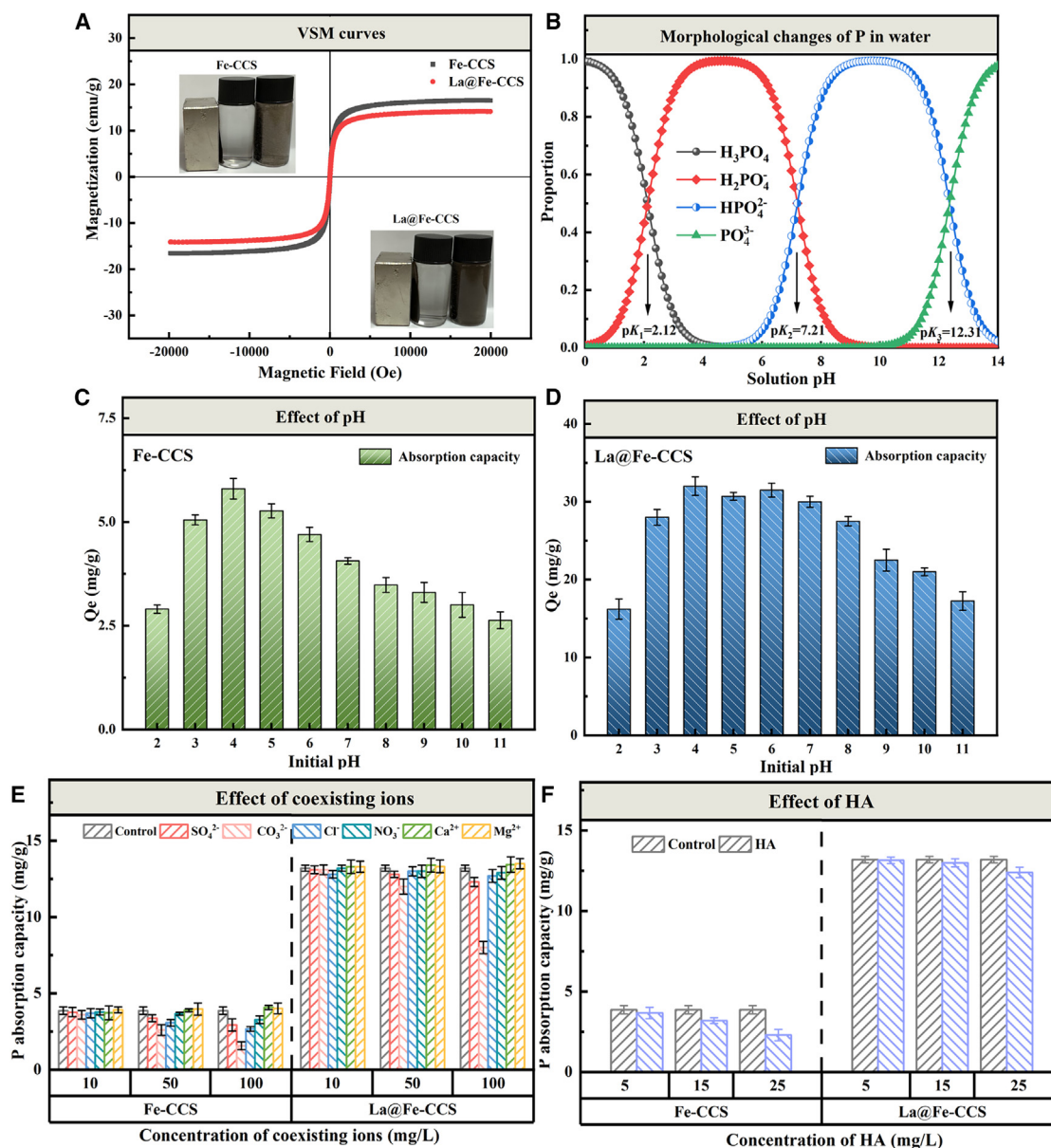
Figure 3. Evaluation of recycling potential and anti-interference ability
(A) VSM curves.
(B) Species distribution of phosphate at different pH levels.
(C–F) Effect of initial pH (C and D) and effect of coexisting ions and HA on phosphate uptake (E and F).
Each experiment in Figure 3. (C–F) was performed three times, and the error bars show ± one standard deviation from the mean of these three trials [n = 3].

for La@Fe-CCS. This is consistent with previous findings; for instance, Zhong et al.[27] and Li et al.[28] reported that CO_3^{2-} decreased the phosphate adsorption capacity of La-MB and La@Fe by approximately 39.41% and 45.81%, respectively. This may be attributed to the strong affinity of La for CO_3^{2-}, which results in the displacement of adsorbed phosphate from the surface of the adsorbent by CO_3^{2-} to form $La_2(CO_3)_3$, thereby interfering with phosphate adsorption. Alternatively, this phenomenon may result from the hydrolysis of high concentrations

of CO_3^{2-} in water, which generates OH^-, thereby increasing the pH and weakening the electrostatic attraction between the adsorbent and phosphate. Interestingly, the presence of Ca^{2+} and Mg^{2+} enhanced phosphate adsorption rather than inhibiting it. This phenomenon may originate from the creation of negatively charged phosphate complexes that adsorbed Ca^{2+} and Mg^{2+}, which then provide additional adsorption sites for phosphate (Equations 13 and 14). Figure 3F indicates that when the humic acid concentration is below 15 mg/L, its effect
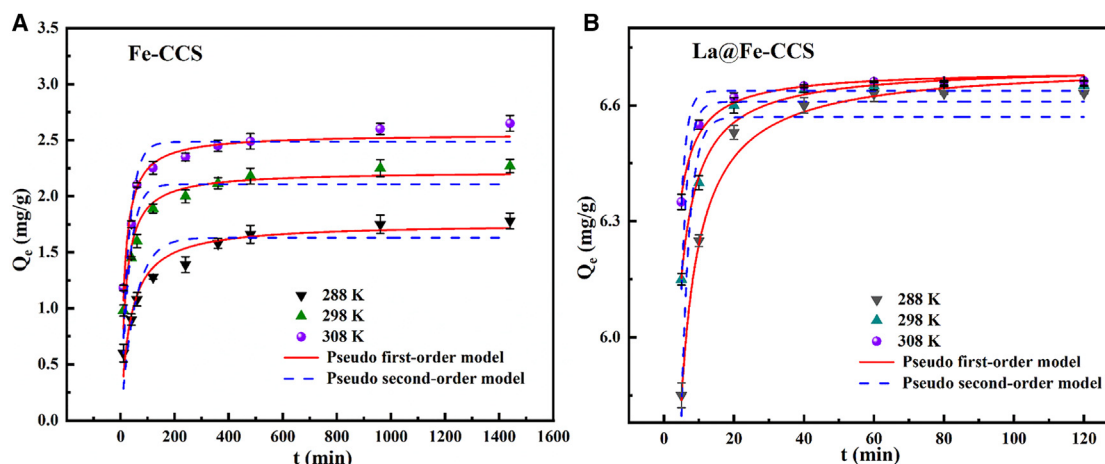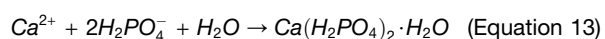
Figure 4. Adsorption kinetic curves
(A) Fe-CCS.
(B) La@Fe-CCS.
Each experiment in Figure 4 was performed three times, and the error bars show ± one standard deviation from the mean of these three trials [n = 3].

on adsorption is minimal; however, at a concentration of 25 mg/L, there is a significant decline in the adsorption capacity of both adsorbents, likely due to the occupation of adsorption sites. Nevertheless, La@Fe-CCS maintains a high adsorption capacity of 12.45 mg/g, significantly exceeding that of Fe-CCS (2.31 mg/g). Prior research on La-based adsorbents has also demonstrated that these materials exhibit strong resistance to a wide range of organic matters.[29]

Based on the aforementioned results, it is evident that La@Fe-CCS faces challenges in high alkaline environments and in the presence of carbonate ions, despite its wide pH adaptability range and excellent anti-interference ability. In a recent study, Jiang et al.[30] reported similar findings when investigating the effects of pH and coexisting ions on La/Fe-MOF. These issues must be considered when designing La-based adsorbents in the future to ensure their adaptation to water bodies with more complex qualities, thereby enhancing the application prospects of this type of adsorbent、

$$Ca^{2+} + 2H_2PO_4^- + H_2O \rightarrow Ca(H_2PO_4)_2 \cdot H_2O \quad \text{(Equation 13)}$$

$$Mg^{2+} + 2H_2PO_4^- \rightarrow Mg(H_2PO_4)_2 \quad \text{(Equation 14)}$$

Adsorption kinetics

The time needed to achieve adsorption equilibrium is a key consideration in developing cost-effective adsorption systems. The kinetic fitting models for Fe-CCS and La@Fe-CCS, presented in Figure 4, reveal distinct adsorption behaviors. At 288 K, 298 K, and 308 K, Fe-CCS adsorption is primarily occurred within the first 480 min, after which the adsorption rate significantly decreased, with saturation achieved at approximately 960 min. In contrast, La@Fe-CCS exhibited rapid adsorption in the initial stages, attaining 95.26%, 98.04%, and 99.12% of its equilibrium adsorption capacity within 20 min. The rapid adsorption of phosphate by La@Fe-CCS, compared to Fe-CCS, may be attributed to the role of Fe in optimizing the electronic structure of La, enhancing the use of La active sites, thus accelerating the adsorption kinetics.[31] Table 2 provides kinetic parameters, demonstrating that the second-order model offered the best fit for both adsorbents at different temperatures, suggesting that chemisorption was the dominant mechanism for phosphate adsorption by both Fe-CCS and La@Fe-CCS.[32] Additionally, the k_2 values for both materials increase with temperature (Fe-CCS: 0.0190, 0.0246, 0.0281; La@Fe-CCS: 0.2001, 0.3352, 0.5743), indicating that higher temperatures are favorable for reducing the time required for adsorption equilibrium, which is consistent with previous reports in the literature.[33]

Table 2. Kinetic parameters of Fe-CCS and La@Fe-CCS adsorption

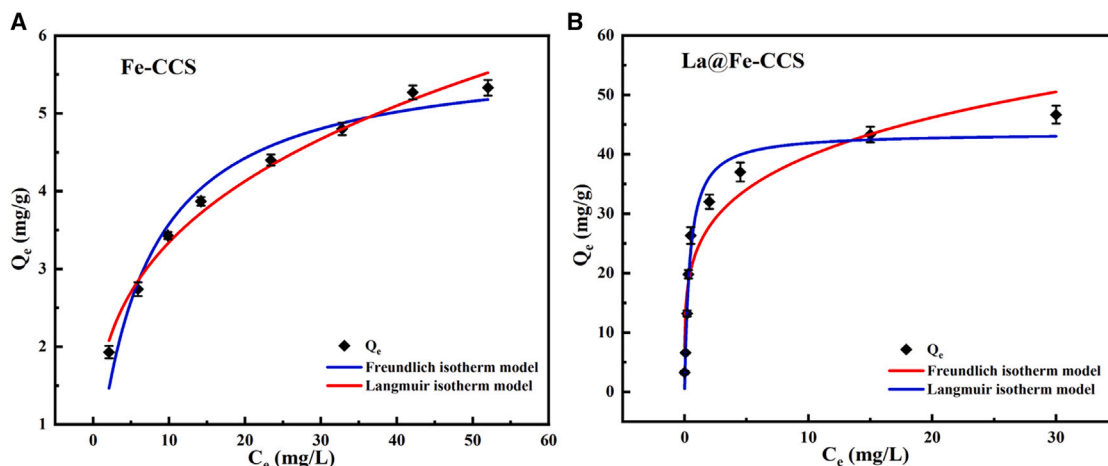| Absorbents	T (K)	First-order model			Second-order model		
		k_1 (1/min)	q_e (mg/g)	R^2	k_2 (g/(mg·min))	q_e (mg/g)	R^2
Fe-CCS	288	0.0334	1.63	0.8359	0.0190	1.76	0.9463
	298	0.0356	2.07	0.8218	0.0246	2.22	0.9732
	308	0.0361	2.49	0.8490	0.0281	2.56	0.9720
La@Fe-CCS	288	0.4277	6.57	0.8426	0.2001	6.67	0.9798
	298	0.5225	6.61	0.7989	0.3352	6.68	0.9833
	308	0.6233	6.64	0.8809	0.5843	6.70	0.9797

Figure 5. Adsorption isotherms
(A) Fe-CCS.
(B) La@Fe-CCS.
Each experiment in Figure 5 was performed three times, and the error bars show ± one standard deviation from the mean of these three trials [$n = 3$].

Adsorption isotherms

Adsorption isotherms provide critical insight into the performance of adsorbents. Figure 5 presents the adsorption properties of Fe-CCS and La@Fe-CCS under varying initial concentrations of phosphate. The adsorption capacity of Fe-CCS dropped with increasing initial phosphate concentration, reaching a maximum adsorption capacity of 5.33 mg/g. In contrast, La@Fe-CCS exhibited a steady increase in adsorption capacity with rising phosphate concentrations, eventually reaching saturation at higher concentrations.

To gain deeper insights into the adsorption mechanisms, the data were explored using the Langmuir and Freundlich isotherm models, and the corresponding results are outlined in Table 3. For Fe-CCS, the Freundlich model provided a better fit ($R^2 = 0.9869$), indicating that the adsorption process involved multilayer adsorption, consistent with observations for other Fe-based materials.[34] In contrast, the Langmuir model better described phosphate adsorption by La@Fe-CCS, as indicated by an R^2 value of 0.9670, implying that the adsorption occurred in a monolayer pattern. According to the Langmuir model, the theoretical maximum adsorption capacity of La@Fe-CCS was estimated at 43.61 mg/g, which is substantially greater than the 5.79 mg/g capacity of Fe-CCS. This marked improvement in adsorption capacity following La modification underscores the efficacy of La@Fe-CCS as a phosphate adsorbent. Notably, the theoretical adsorption capacity of La@Fe-CCS exceeded that of many La-modified materials (Table 4), highlighting its potential as a highly efficient adsorbent. In addition, we assessed the synthesis cost of La@Fe-CCS. According to market

prices, the cost of the primary raw materials for synthesizing La@Fe-CCS is approximately 24.02 USD/kg. Although this cost is lower than that of most La-based materials, it remains relatively high in comparison to La-Z (9.08 USD/kg). This cost level may restrict the commercialization potential of La@Fe-CCS. Therefore, to enhance the feasibility of La@Fe-CCS in practical applications, optimizing the synthesis process to reduce costs will be one of the primary focuses of our future research.

Adsorption thermodynamics

The effect of temperature on the adsorption capacity of the adsorbents is illustrated in Figure 6A. The results showed that the adsorption capacity of Fe@CCS and La@Fe-CCS increased with the increase in temperature rose from 288 K to 308 K. This suggested that higher temperatures favor for enhancing the phosphate uptake capacity by the materials.[20] Further analysis of the adsorption thermodynamic data presented in Figure 6B yields thermodynamic parameters, summarized in Table 5. The ΔG^0 value for Fe@CCS was positive, indicating non-spontaneous behavior in the adsorption process. This finding is consistent the results of a previous study on Fe-based biochar (Fe@WBC).[40] In contrast, the ΔG^0 value for La@Fe-CCS was negative, suggesting that the phosphate adsorption reaction on La@Fe-CCS was spontaneous, a behavior commonly observed in La-based materials.[41] The positive ΔH^0 values for both Fe@CCS (20.69 kJ/mol) and La@Fe-CCS (51.41 kJ/mol) indicated that phosphate adsorption by both materials was endothermic. Furthermore, the positive ΔS^0 values for

Table 3. Isotherm parameters of Fe-CCS and La@Fe-CCS adsorption

Absorbents	T (°C)	Langmuir model				Freundlich model		
		q_m (mg/g)	K_L (L/mg)	R_L	R^2	K_F	1/n	R^2
Fe-CCS	25	5.79	0.1612	0.0937	0.9579	1.66	0.3047	0.9869
La@Fe-CCS	25	43.61	2.4102	0.0042	0.9670	23.92	0.2197	0.9061

Table 4. Comparison of La-based absorbents for phosphate removal capacity

| Materials	Adsorption capacity (mg/g)	Initial concentration (mg/L)	Contact time (min)	pH adaptation range	Temperature (°C)	Dosage (g/L)	Cost USD/kg	Reference
La@Fe-CCS	43.61	5–100	20	3–8	25	1.5	24.02	This Work
$Fe_3O_4@SiO_2@La_2O_3$	27.8	0–200	10	5–9	25	1	32.55	Lai et al.[35]
La-Z	17.2	5–60	240	3–7	40	2	9.08	He et al.[36]
La-Zr@FeO	49.1	0–50	60	2–6	25	0.25	69.66	Lin et al.[37]
MLC-10	19.34	0–15	120	5–9	25	0.2	21.06	Song et al.[38]
SAILa@AB	21.30	10–1000	30	4–7	25	10	37.98	Yin et al.[39]

Fe@CCS (51.70 J/(mol·K)) and La@Fe-CCS (194.77 J/(mol·K)) indicated that phosphate adsorption by both materials progressed in the direction of increasing entropy, suggesting that the system became more disordered as the adsorption reaction progressed.

FTIR

Figure 7 presents the FTIR spectra of CS, CCS, Fe-CCS, and La@Fe-CCS. The spectrum of CS (Figure 7A) reveals several distinct vibrational peaks: carbonate compounds are indicated by a peak near 2515 cm^{-1}; C=O bonding in bicarbonate ions appears around 1800 cm^{-1}; and C-O stretching vibrational modes in carbonate groups correspond to peaks at 875 cm^{-1} and 711 cm^{-1}.[42] Additionally, a characteristic peak near 1422 cm^{-1} is attributed to CO_3^{2-} ions. These observations suggest that CS mainly consists of calcium carbonate, consistent with the results of the previous XRD analysis. After calcination, CCS exhibited similar peaks to CS, although they were notably weakened, indicating partial loss of $CaCO_3$ during the process, which aligns with the XRD results. Following the loading of Fe and Fe/La, new features emerged: O-H bonds were observed near 3406 cm^{-1} and 1620 cm^{-1}, corresponding to stretching vibrations of adsorbed or bound hydroxyl groups. The characteristic peak of Fe-OH appeared around 790 cm^{-1}, and peaks at 667 and 559 cm^{-1} may originate from Fe-O bonds. These findings are consistent with the results of You et al.,[29] confirming that both materials were successfully loaded with Fe. For La@Fe-CCS, new peaks at 1483 and 1386 cm^{-1}, caused by La-OH bond vibrations, correspond with the experiments,[28,43] indicating the loading of lanthanum hydroxide onto the surface of La@Fe-CCS. The small peak observed near 858 cm^{-1} may be attributed to La-O.[44]

Figure 7B illustrates the FTIR spectra of Fe-CCS and La@Fe-CCS, demonstrating that the –OH peak in Fe-CCS weakened after phosphate adsorption, while it nearly disappeared in La@Fe-CCS. This attenuation is attributed to the involvement of –OH groups in the phosphate uptake process.[45] Peaks appeared at 1095 cm^{-1} for Fe-CCS and 1060 cm^{-1} for La@Fe-CCS, corresponding to asymmetric vibrational peaks of the P-O bond, confirming successful phosphate adsorption by both materials. The peaks associated with Fe-OH and Fe-O in Fe-CCS diminished or disappeared after adsorption, reflecting the creation of a Fe-P complex.[46] Similar changes occurred for Fe-OH and Fe-O in La@Fe-CCS, with the peaks of La-OH and La-O nearly completely disappearing after adsorption,
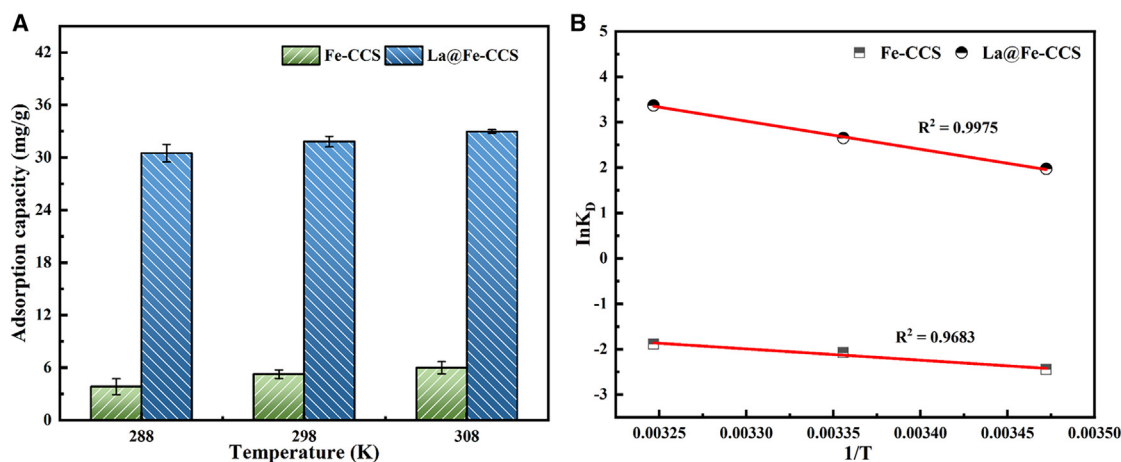
Figure 6. Thermodynamic analysis
(A) Effect of temperature on adsorption capacity.
(B) Graphical representation of thermodynamic constants.
Experiment in Figure 6A was performed three times, and the error bars show ± one standard deviation from the mean of these three trials [n = 3].

Table 5. Isotherm parameters of Fe-CCS and La@Fe-CCS adsorption

Absorbents	ΔG^0(KJ/mol)			ΔH^0(KJ/mol)	ΔS^0(J/(mol·K))
	288K	298K	308K		
Fe-CCS	5.86	5.18	4.83	20.69	51.70
La@Fe-CCS	−4.72	−6.56	−8.62	51.41	194.77

suggesting an intrasphere complexation reaction involving Fe/La during the adsorption process. A new peak around 627 cm^{-1}, corresponding to the O-P-O bond bending vibration, was detected, further validating the interaction between phosphate and the adsorbents.[41]

XPS

The reaction mechanisms during the adsorption of Fe-CCS and La@Fe-CCS were further investigated using XPS (Figure 8). Before adsorption, the Fe signal in the spectrum of Fe-CCS was evident (Figure 8A), confirming the effective loading of Fe onto the Fe-CCS surface. Following adsorption, the detection of the P signal confirmed the effective capture of phosphate by Fe-CCS. The Fe 2p$_{3/2}$ and Fe 2p$_{1/2}$ peaks prior to adsorption were recorded at 710.9 eV and 724.4 eV, respectively (Figure 8B). After adsorption, these peaks shifted to 710.5 eV and 724.1 eV, indicating an interaction between Fe and P that likely resulted in the creation of Fe-O-P intrasphere complexes.[47] The P 2p peak of adsorbed P on Fe-CCS was detected at 133.5 eV, compared to KH_2PO_4 (134.0 eV) (Figure 8C). This peak, which shifted to a lower binding energy but was close to the reference sample $FePO_4 \cdot 2H_2O$ (133.6 eV),[48] further indicates that ligand exchange between Fe and P occurred, forming Fe-P complexes. The O 1s photoelectron spectroscopy data for Fe-CCS (Figure 8D) were deconvoluted to identify the M-O (metal-oxygen), M-OH (hydroxyl), and H_2O (adsorbed water) peaks. After

phosphate adsorption, the M-OH peak area decreased from 50.69% to 45.39%, while the M-O peak area increased from 22.09% to 37.24%. This suggests that Fe-OH on the Fe-CCS surface plays a key role in phosphate adsorption, with -OH being replaced by phosphate during the process.

The XPS analysis of La@Fe-CCS is shown in Figures 8E–8I. Before adsorption, the wide scanning of elemental composition images confirmed the loading of La and Fe onto the La@Fe-CCS surface. After adsorption, the P signal appeared, indicating effective phosphate capture. The binding energies of La 3d$_{5/2}$ and La 3d$_{3/2}$ were 835.2 eV and 851.9 eV before adsorption, respectively (Figure 8E). After adsorption, these shifted to higher binding energies by 0.5 eV and 0.3 eV, respectively, suggesting a valence band transfer of La during adsorption and the formation of La-O-P intrasphere complexes.[49] Compared to Fe-CCS, the Fe 2p$_{3/2}$ (724.3 eV) and Fe 2p$_{1/2}$ (710.8 eV) peaks of La@Fe-CCS shifted only slightly (0–0.1 eV) after phosphate adsorption, indicating that only a small amount of Fe was involved in forming intrasphere ferric phosphate complexes. The P 2p peak, centered at 133.4 eV, was significantly shifted to a lower binding energy compared to KH_2PO_4 (134.0 eV), reflecting a strong affinity of La@Fe-CCS for phosphate. The proximity of this peak to reference samples $FePO_4 \cdot 2H_2O$ (133.6 eV) and $LaPO_4 \cdot 2H_2O$ (132.8 eV) further confirms the formation of Fe-P or La-P complexes.[48] In addition, some close H_3PO_4 analogs (134.4 eV) were identified, suggesting precipitation as one of the pathways for the phosphate removal by La@Fe-CCS.[50] After phosphate adsorption, the relative area ratio of the M-O peaks increased from 17.58% to 30.52%, while the relative area ratio of the La-OH peaks decreased from 60.85% to 48.18%. This indicated that ligand exchange involving La-adsorbed hydroxyl group (La-O-H) and a small amount of Fe-adsorbed hydroxyl groups (Fe-O-H) with phosphate anions, along with the creation of La-O-P/Fe-O-P bonds, is crucial for the adsorption of phosphate
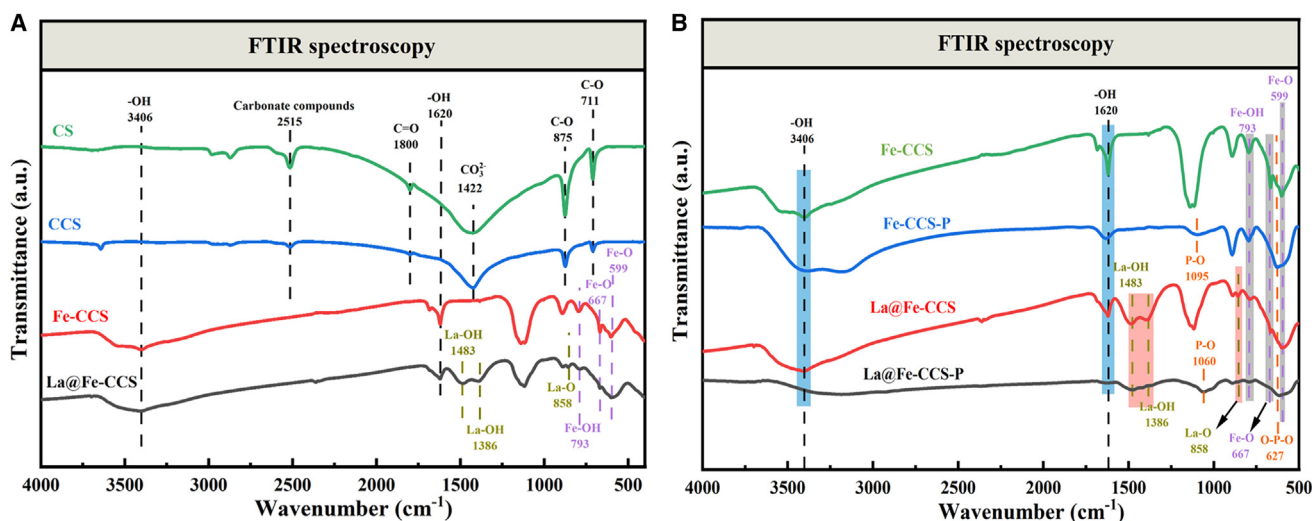

Figure 7. FTIR spectra of CS, CCS, Fe-CCS, and La@Fe-CCS
(A) CS, CCS, Fe-CCS, and La@Fe-CCS before phosphate adsorption.
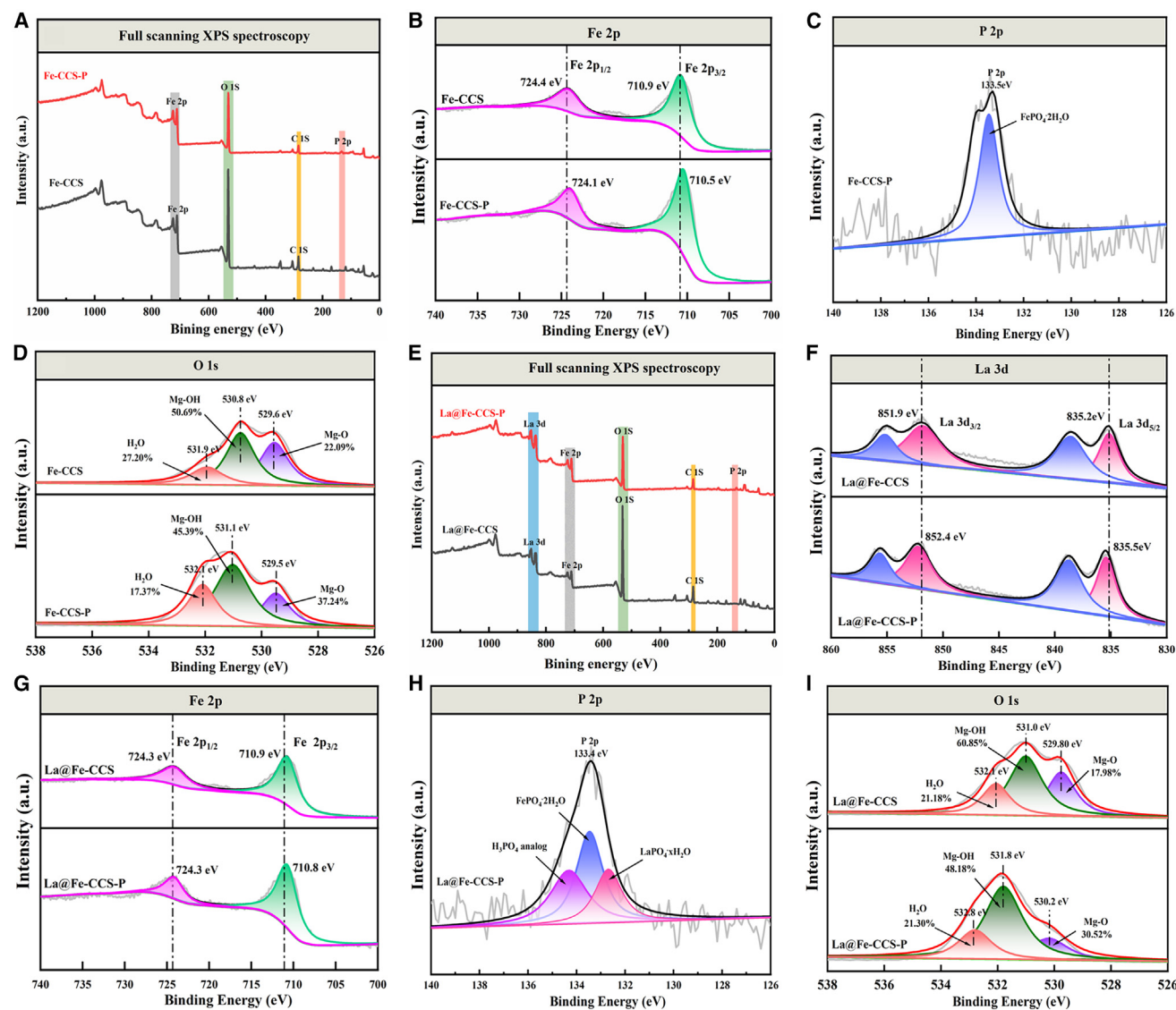(B) Fe-CCS and La@Fe-CCS before and after phosphate adsorption.

Figure 8. XPS spectra
(A–D) Fe-CCS.
(E–I) La@Fe-CCS.

by La@Fe-CCS.[51] Figure 9 illustrates the potential removal mechanisms involved in the phosphate removal process of La-Fe@CCS.

Examination of continuous regeneration performance of La@Fe-CCS

The cyclic regeneration capacity is a crucial indicator for assessing the performance of recyclable magnetic adsorbents. Previous results showed that La@Fe-CCS exhibited significantly better adsorption performance compared to Fe-CCS, making it the preferred choice for further testing. Figure 10A presents the adsorption capacity and desorption rate of phosphate for La@Fe-CCS over five regeneration cycles. La@Fe-CCS maintained its phosphate adsorption capacity well after

the first cycle, demonstrating an adsorption capacity of 31.40 mg/g, with only a 1.20% decrease in the removal rate. The adsorption capacity exhibited a significant decrease following the second cycle, with the removal rate declining by 9.30%; subsequently, the adsorption capacity continued to decline with an increasing number of cycles. Nevertheless, even after five cycles, the removal rate remained high at 75.3%. The slight decrease in adsorption efficiency could be attributed to factors such as aggregation, agglomeration, or precipitate formation on the material surface, which may have reduced the number of active adsorption sites. To minimize this loss, selecting appropriate desorption conditions may be a wise choice, including the type, concentration, and pH of the desorption solution. Notably, La@Fe-CCS consistently
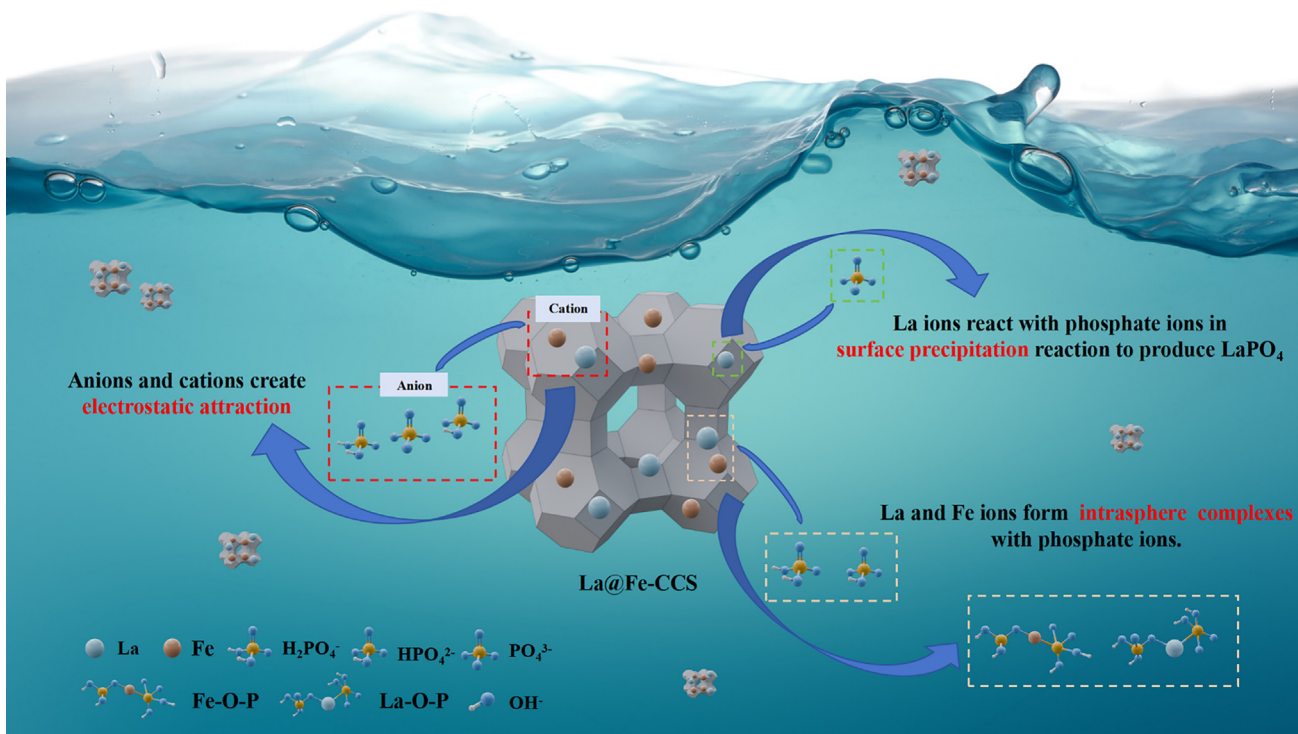
Figure 9. The mechanism chart of phosphate adsorption by La@Fe-CCS

achieved a resolution rate exceeding 71.0% in each cycle across all five cycles, indicating its strong capacity for phosphate recovery even after multiple uses. These results confirm that La@Fe-CCS is a highly effective and cost-efficient adsorbent.

Treatment of real sewage

To combat eutrophication in water bodies, it is essential to limit phosphate levels in municipal sewage discharge. Therefore, this study further explored the phosphate removal capacity of La@Fe-CCS in real domestic sewage to assess its practical application. The untreated sewage had the following characteristics: pH = 6.88, COD = 396.0 mg/L, TN = 29.2 mg/L, NH_4^+-N = 17.5 mg/L, and TP = 6.2 mg/L. Figure 10B illustrates a significant reduction in the concentrations of these contaminants following treatment with La@Fe-CCS. Specifically, removal rates of over 55% were achieved for COD, TN, and NH_4+-N, with final concentrations of 159.3 mg/L, 12.5 mg/L, and 7.6 mg/L, respectively. Importantly, the TP concentration decreased to 0.22 mg/L, well below the Class IV environmental quality
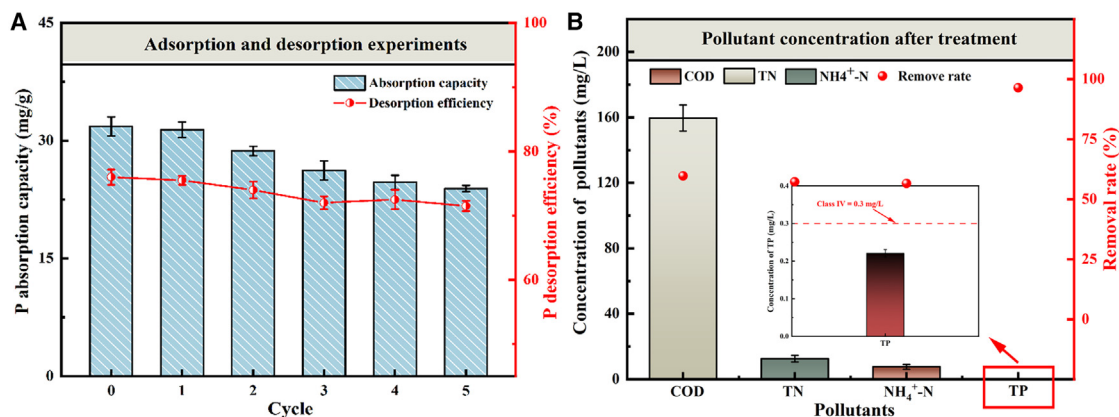

Figure 10. La@Fe-CCS cycle recycling performance and sewage treatment capacity
(A) Recirculation experiments.
(B) Treated effluent pollutant concentrations.
Each experiment Figure 10 was performed three times, and the error bars show ± one standard deviation from the mean of these three trials [n = 3].

standard for surface water (TP = 0.3 mg/L). However, the removal efficiency of La@Fe-CCS in real sewage was lower than that observed with laboratory-prepared phosphate solutions, likely due to the more complex composition of domestic sewage.

Conclusions

La@Fe-CCS materials were synthesized for the adsorption and recovery of phosphate from water. SEM-EDS, XRD, and VSM analyses confirmed that magnetite and lanthanum hydroxide were successfully loaded onto the surface of La@Fe-CCS, and that La@Fe-CCS can be efficiently recovered using an external magnetic field. La@Fe-CCS showed excellent adsorption capacity over a broad pH range (3–8) and displayed a high degree of selectivity for phosphate, even in the presence of competing ions and humic acid. La@Fe-CCS outperformed Fe-CCS in adsorption kinetics and capacity, reaching saturation within approximately 20 min with a maximum theoretical capacity of 43.61 mg/g. FTIR and XPS analyses indicated that ligand-exchanged intrasphere complexation was the primary mechanism driving phosphate adsorption in La@Fe-CCS. Moreover, La@Fe-CCS retained more than 75.3% adsorption efficiency and a resolution rate of 71.0% after five phosphate adsorption/desorption cycles. When applied to domestic sewage, La@Fe-CCS effectively reduced the TP concentration from 6.2 mg/L to 0.22 mg/L.

Limitations of the study

Despite the high efficiency of La@Fe-CCS in removing phosphate from domestic sewage, certain challenges remain. Various pollutants are present in natural water bodies, and this study focuses solely on the phosphate removal potential of La@Fe-CCS. The investigation of La@Fe-CCS was limited to laboratory conditions, and no pilot-scale experiments have been conducted to assess its performance in sewage treatment. Therefore, future research will focus on optimizing the preparation process of La@Fe-CCS, exploring synergistic treatment methods for other pollutants, and evaluating its long-term stability.

RESOURCE AVAILABILITY

Lead contact

Further information and requests for resources should be directed to and will be fulfilled by the lead contact, Hui Luo (water@njfu.edu.cn).

Materials availability

All the raw materials used in this study are commercially available.

Data and code availability

- The datasets used and/or analyzed during the current study are available from the lead contact upon reasonable request.
- No codes were used in this study.

AUTHOR CONTRIBUTIONS

Conceptualization, H.L. and H.W.; methodology, Z.J.; software, B.-J.H.; validation, B.-J.H.; formal analysis, H.W.; investigation, T.Q., M.T., and L.C; resources, H.L.; data curation, J.Y.; writing—original draft preparation, H.W.; writing—review and editing, H.L. and J.Y.; visualization, B.-J.H. and M.L.; supervision, H.L.; project administration, H.L.; funding acquisition, H.L. All authors have read and agreed to the published version of the manuscript.

DECLARATION OF INTERESTS

The authors declare no competing interests.

STAR★METHODS

Detailed methods are provided in the online version of this paper and include the following:

- KEY RESOURCES TABLE
- METHOD DETAILS
  - Raw materials
  - Material properties
  - CS powder pretreatment
  - Preparation of La@Fe-CCS and Fe-CCS
  - Adsorption tests
  - Cyclic regeneration and practical application
- QUANTIFICATION AND STATISTICAL ANALYSIS

SUPPLEMENTAL INFORMATION

Supplemental information can be found online at https://doi.org/10.1016/j.isci.2025.111762.

REFERENCES

1. Asikin-Mijan, N., Taufiq-Yap, Y., and Lee, H. (2015). Synthesis of clamshell derived Ca(OH)$_2$ nano-particles via simple surfactant-hydration treatment. Chem. Eng. J. *262*, 1043–1051. https://doi.org/10.1016/j.cej.2014.10.069.

2. Wang, Q., Gao, W., Wang, Z., and Lyu, X. (2022). Effect of clam shell from kitchen waste on the synthesis, performance, and hydration of cementitious clinker. Construct. Build. Mater. *323*, 126588. https://doi.org/10.1016/j.conbuildmat.2022.126588.

3. Liang, Y., Zhao, Q., Li, X., Zhang, Z., and Ren, L. (2016). Study of the microstructure and mechanical properties of white clam shell. Micron *87*, 10–17. https://doi.org/10.1016/j.micron.2016.04.007.

4. Liang, J., Huang, Z., Liu, J., Lin, S., Lin, Z., Evrendilek, F., Xie, W., Zhuang, G., He, Y., Wang, L., and Yang, C. (2024). Multiplicative effects of co-incineration of sewage sludge and wasted oyster shells in air, CO$_2$, and steam atmospheres on P speciation and bioavailability and metal ecotoxicity. Chem. Eng. J. *490*, 151683. https://doi.org/10.1016/j.cej.2024.151683.

5. Arun, J., Gopinath, K.P., SundarRajan, P., Malolan, R., Adithya, S., Sai Jayaraman, R., and Srinivaasan Ajay, P. (2020). Hydrothermal liquefaction of Scenedesmus obliquus using a novel catalyst derived from clam shells: Solid residue as catalyst for hydrogen production. Bioresour. Technol. *310*, 123443. https://doi.org/10.1016/j.biortech.2020.123443.

6. Narayan, R.B., Goutham, R., Srikanth, B., and Gopinath, K. (2018). A novel nano-sized calcium hydroxide catalyst prepared from clam shells for the photodegradation of methyl red dye. J. Environ. Chem. Eng. 6, 3640–3647. https://doi.org/10.1016/j.jece.2016.12.004.

7. Niju, S., Begum, K.M.S., and Anantharaman, N. (2016). Enhancement of biodiesel synthesis over highly active CaO derived from natural white bivalve clam shell. Arab. J. Chem. 9, 633–639. https://doi.org/10.1016/j.arabjc.2014.06.006.

8. Núñez, D., Serrano, J.A., Mancisidor, A., Elgueta, E., Varaprasad, K., Oyarzún, P., Cáceres, R., Ide, W., and Rivas, B.L. (2019). Heavy metal removal from aqueous systems using hydroxyapatite nanocrystals derived from clam shells. RSC Adv. 9, 22883–22890. https://doi.org/10.1039/C9RA04198B.

9. Ren, Z., Zeng, W., Liu, H., Jia, Y., Peng, X., and Peng, Y. (2021). Enhanced bioavailability of phosphorus in sewage sludge through pyrolysis aided by calcined clam shell powder. Process Saf. Environ. Protect. 156, 121–133. https://doi.org/10.1016/j.psep.2021.10.008.

10. Brakemi, E., Michael, K., Tan, S.P., and Helen, H. (2023). Phosphate removal from wastewater using scallop and whelk shells. J. Water Process Eng. 55, 104159. https://doi.org/10.1016/j.jwpe.2023.104159.

11. d'Haese, P.C., Douglas, G., Verhulst, A., Neven, E., Behets, G.J., Vervaet, B.A., Finsterle, K., Lürling, M., and Spears, B. (2019). Human health risk associated with the management of phosphorus in freshwaters using lanthanum and aluminium. Chemosphere 220, 286–299. https://doi.org/10.1016/j.chemosphere.2018.12.093.

12. Wu, B., Fang, L., Fortner, J.D., Guan, X., and Lo, I.M.C. (2017). Highly efficient and selective phosphate removal from wastewater by magnetically recoverable La(OH)$_3$/Fe$_3$O$_4$ nanocomposites. Water Res. 126, 179–188. https://doi.org/10.1016/j.watres.2017.09.034.

13. Nguyen, T.A.H., Ngo, H.H., Guo, W.S., Nguyen, T.H.H., Vu, N.D., Soda, S., Nguyen, T.T., Nguyen, M.K., Tran, T.V.H., Dang, T.T., et al. (2020). White hard clam (Meretrix lyrata) shells as novel filter media to augment the phosphorus removal from wastewater. Sci. Total Environ. 741, 140483. https://doi.org/10.1016/j.psep.2021.10.008.

14. Souza, T.A., Mascarenhas, A.J.S., Andrade, H.M.C., and Santos, T.S.M. (2018). Combining sewage sludge and clam shell waste to prepare adsorbents for efficient phosphorous removal. Water Air Soil Pollut. 229, 383. https://doi.org/10.1007/s11270-018-4029-1.

15. Khan, M.D., Chottitisupawong, T., Vu, H.H.T., Ahn, J.W., and Kim, G.M. (2020). Removal of phosphorus from an aqueous solution by nanocalcium hydroxide derived from waste bivalve seashells: mechanism and kinetics. ACS Omega 5, 12290–12301. https://doi.org/10.1021/acsomega.0c00993.

16. Yin, H., Liu, L., Lv, M., Feng, L., and Zhou, J. (2020). Metal-modified mussel shell for efficient binding of phosphorus in eutrophic waters. Int. J. Environ. Res. 14, 135–143. https://doi.org/10.1007/s41742-020-00250-9.

17. Fu, H., Yang, Y., Zhu, R., Liu, J., Usman, M., Chen, Q., and He, H. (2018). Superior adsorption of phosphate by ferrihydrite-coated and lanthanum-decorated magnetite. J. Colloid Interface Sci. 530, 704–713. https://doi.org/10.1016/j.jcis.2018.07.025.

18. Irfan, I., Inam, M.A., and Iftikhar, R. (2024). Comparative phosphate sorption and recovery potential of mono and bimetallic iron-lanthanum impregnated biochar derived via co-pyrolysis of sewage sludge and wheat straw: Highly effective phosphatic fertilizer. J. Water Process Eng. 66, 106110. https://doi.org/10.1016/j.jwpe.2024.106110.

19. Wang, Y., Lin, J.W., Zhan, Y.H., Zhang, H.H., Zhang, Z.B., He, S.Q., Zhao, Y.Y., Wu, X.L., and Yu, Y. (2019). Effect of magnetic zirconium/iron-modified bentonite addition on phosphorus mobilization and species transformation in river sediments. Environ. Sci. 40, 649–657. https://doi.org/10.13227/j.hjkx.201806220.

20. Liu, S., Zhao, S., Fan, F., Zhang, B.-T., and Wang, S. (2022). Magnetically separable and recyclable lanthanum/iron co-modified attapulgite: A sustainable option to efficiently control phosphate loading. J. Clean. Prod. 348, 131294. https://doi.org/10.1016/j.jclepro.2022.131294.

21. Lan, Z., Lin, Y., and Yang, C. (2022). Lanthanum-iron incorporated chitosan beads for adsorption of phosphate and cadmium from aqueous solutions. Chem. Eng. J. 448, 137519. https://doi.org/10.1016/j.cej.2022.137519.

22. Zhou, Z., Yan, J., Wu, Z., Xu, Q., Fang, X., Zhong, Q., and Li, Q. (2023). Preparation and characterization of abandoned oyster shell-metal materials and their adsorption and mechanism of phosphorus in wastewater. Mater. Today Sustain 24, 100531. https://doi.org/10.1016/j.mtsust.2023.100531.

23. He, Y., Lin, H., Dong, Y., Li, B., Wang, L., Chu, S., Luo, M., and Liu, J. (2018). Zeolite supported Fe/Ni bimetallic nanoparticles for simultaneous removal of nitrate and phosphate: synergistic effect and mechanism. Chem. Eng. J. 347, 669–681. https://doi.org/10.1016/j.cej.2018.04.088.

24. Luo, Q., Wei, J., Guo, Z., and Song, Y. (2024). Adsorption and immobilization of phosphorus from water and sediments using a lanthanum-modified natural zeolite: Performance, mechanism and effect. Sep. Purif. Technol. 329, 125187. https://doi.org/10.1016/j.seppur.2023.125187.

25. Lin, J., Zhao, Y., Zhan, Y., and Wang, Y. (2020). Control of internal phosphorus release from sediments using magnetic lanthanum/iron-modified bentonite as active capping material. Environ. Pollut. 264, 114809. https://doi.org/10.1016/j.envpol.2020.114809.

26. Luo, Q., Zhang, X., Wei, J., Zhang, J., Guo, Z., and Song, Y. (2025). High-efficiency lanthanum-modified zeolite adsorbents for phosphorus control and algal suppression: Preparation, characterization and mechanistic insights. Sep. Purif. Technol. 352, 128146. https://doi.org/10.1016/j.seppur.2024.128146.

27. Zhong, Z., Lu, X., Yan, R., Lin, S., Wu, X., Huang, M., Liu, Z., Zhang, F., Zhang, B., Zhu, H., and Guo, X. (2020). Phosphate sequestration by magnetic La-impregnated bentonite granules: A combined experimental and DFT study. Sci. Total Environ. 738, 139636. https://doi.org/10.1016/j.scitotenv.2020.139636.

28. Li, G., Zhang, Y., Hu, X., Wei, T., Li, J., Hongbin, W., and Wang, X. (2024). A study on the performance of a recyclable adsorbent La@Fe for phosphate adsorption in wastewater. Process Saf. Environ. Protect. 188, 25–38. https://doi.org/10.1016/j.psep.2024.05.075.

29. You, K., Yang, W., Song, P., Fan, L., Xu, S., Li, B., and Feng, L. (2022). Lanthanum-modified magnetic oyster shell and its use for enhancing phosphate removal from water. Colloids Surf., A 633, 127897. https://doi.org/10.1016/j.colsurfa.2021.127897.

30. Jiang, X., Su, S., Ren, B., Qiu, Y., Wang, S., and Yang, X. (2025). Lanthanum-Doped iron MOFs: A sustainable solution for Arsenic (V) and phosphate pollution in water. Sep. Purif. Technol. 354, 129098. https://doi.org/10.1016/j.seppur.2024.129098.

31. Yu, J., Xiang, C., Zhang, G., Wang, H., Ji, Q., and Qu, J. (2019). Activation of lattice oxygen in LaFe (oxy) hydroxides for efficient phosphorus removal. Environ. Sci. Technol. 53, 9073–9080. https://doi.org/10.1021/acs.est.9b01939.

32. Qiu, H., Liang, C., Yu, J., Zhang, Q., Song, M., and Chen, F. (2017). Preferable phosphate sequestration by nano-La (III)(hydr) oxides modified wheat straw with excellent properties in regeneration. Chem. Eng. J. 315, 345–354. https://doi.org/10.1016/j.cej.2017.01.043.

33. Yoon, S.-Y., Lee, C.-G., Park, J.-A., Kim, J.-H., Kim, S.-B., Lee, S.-H., and Choi, J.-W. (2014). Kinetic, equilibrium and thermodynamic studies for phosphate adsorption to magnetic iron oxide nanoparticles. Chem. Eng. J. 236, 341–347. https://doi.org/10.1016/j.cej.2013.09.053.

34. Ajmal, Z., Muhmood, A., Usman, M., Kizito, S., Lu, J., Dong, R., and Wu, S. (2018). Phosphate removal from aqueous solution using iron oxides: adsorption, desorption and regeneration characteristics. J. Colloid Interface Sci. 528, 145–155. https://doi.org/10.1016/j.jcis.2018.05.084.

35. Lai, L., Xie, Q., Chi, L., Gu, W., and Wu, D. (2016). Adsorption of phosphate from water by easily separable Fe3O4@ SiO$_2$ core/shell magnetic nanoparticles functionalized with hydrous lanthanum oxide. J. Colloid Interface Sci. 465, 76–82. https://doi.org/10.1016/j.jcis.2015.11.043.

36. He, Y., Lin, H., Dong, Y., and Wang, L. (2017). Preferable adsorption of phosphate using lanthanum-incorporated porous zeolite: characteristics and mechanism. Appl. Surf. Sci. *426*, 995–1004. https://doi.org/10.1016/j.apsusc.2017.07.272.

37. Lin, X., Xie, Y., Lu, H., Xin, Y., Altaf, R., Zhu, S., and Liu, D. (2021). Facile preparation of dual La-Zr modified magnetite adsorbents for efficient and selective phosphorus recovery. Chem. Eng. J. *413*, 127530. https://doi.org/10.1016/j.cej.2020.127530.

38. Song, Q., Huang, S., Xu, L., Wang, N., Hu, Z., Luo, X., and Zheng, Z. (2020). Synthesis of magnetite/lanthanum hydroxide composite and magnetite/aluminum hydroxide composite for removal of phosphate. Sci. Total Environ. *723*, 137838. https://doi.org/10.1016/j.scitotenv.2020.137838.

39. Yin, H., Zhang, M., Huo, L., and Yang, P. (2022). Efficient removal of phosphorus from constructed wetlands using solidified lanthanum/aluminum amended attapulgite/biochar composite as a novel phosphorus filter. Sci. Total Environ. *833*, 155233. https://doi.org/10.1016/j.scitotenv.2022.155233.

40. Irfan, I., Inam, M.A., Usmani, W., Iftikhar, R., and Jahan, Z. (2023). Adsorptive recovery of phosphate using iron functionalized biochar prepared via co-pyrolysis of wheat straw and sewage sludge. Environ. Technol. Innovat. *32*, 103434. https://doi.org/10.1016/j.eti.2023.103434.

41. Yi, Y., Fu, Y., Wang, Y., Xu, Z., and Diao, Z. (2024). Lanthanum/iron co-modified biochar for highly efficient adsorption of low-concentration phosphate from aqueous solution. J. Environ. Chem. Eng. *12*, 111876. https://doi.org/10.1016/j.jece.2024.111876.

42. Jung, S., Heo, N.S., Kim, E.J., Oh, S.Y., Lee, H.U., Kim, I.T., Hur, J., Lee, G.-W., Lee, Y.-C., and Huh, Y.S. (2016). Feasibility test of waste oyster shell powder for water treatment. Process Saf. Environ. Protect. *102*, 129–139. https://doi.org/10.1016/j.psep.2016.03.004.

43. Li, X., Wang, Y., Li, J., Dong, S., Hao, H., Liu, C., Tong, Y., and Zhou, Y. (2021). Rapid and selective harvest of low-concentration phosphate by La (OH)₃ loaded magnetic cationic hydrogel from aqueous solution: Surface migration of phosphate from -N⁺(CH₃)₃ to La (OH)₃. Sci. Total Environ. *800*, 149418. https://doi.org/10.1016/j.scitotenv.2021.149418.

44. Wang, B., Zhang, H., Hu, X., Chen, R., Guo, W., Wang, H., Wang, C., Yuan, J., Chen, L., and Xia, S. (2023). Efficient phosphate elimination from aqueous media by La/Fe bimetallic modified bentonite: Adsorption behavior and inner mechanism. Chemosphere *312*, 137149. https://doi.org/10.1016/j.chemosphere.2022.137149.

45. Liu, Y., Huang, L., Le, X., and Huang, R. (2024). Performance and mechanism on the phosphorus adsorption by magnetic lanthanum-loaded acidified vermiculite. J. Civ. Environ. Eng. *46*, 197–205. https://doi.org/10.11835/j.issn.2096-6717.2021.247.

46. Zhang, Q., Kang, P., Wang, L., Li, Q., Gong, J., Li, L., Zhang, B., Li, S., and Yang, X. (2024). Controllable fabrication of lanthanum-based metal-organic frameworks for efficient phosphorus recovery from water. J. Mol. Struct. *1299*, 137110. https://doi.org/10.1016/j.molstruc.2023.137110.

47. Chen, Z., Lin, B., Huang, Y., Liu, Y., Wu, Y., Qu, R., and Tang, C. (2023). Pyrolysis temperature affects the physiochemical characteristics of lanthanum-modified biochar derived from orange peels: Insights into the mechanisms of tetracycline adsorption by spectroscopic analysis and theoretical calculations. Sci. Total Environ. *862*, 160860. https://doi.org/10.1016/j.scitotenv.2022.160860.

48. Wu, Y., Li, X., Yang, Q., Wang, D., Xu, Q., Yao, F., Chen, F., Tao, Z., and Huang, X. (2019). Hydrated lanthanum oxide-modified diatomite as highly efficient adsorbent for low-concentration phosphate removal from secondary effluents. J. Environ. Manag. *231*, 370–379. https://doi.org/10.1016/j.jenvman.2018.10.059.

49. Liao, T., Li, T., Su, X., Yu, X., Song, H., Zhu, Y., and Zhang, Y. (2018). La (OH)₃-modified magnetic pineapple biochar as novel adsorbents for efficient phosphate removal. Bioresour. Technol. *263*, 207–213. https://doi.org/10.1016/j.biortech.2018.04.108.

50. Wang, Z., Shen, D., Shen, F., and Li, T. (2016). Phosphate adsorption on lanthanum loaded biochar. Chemosphere *150*, 1–7. https://doi.org/10.1016/j.chemosphere.2016.02.004.

51. Sun, E., Zhang, Y., Xiao, Q., Li, H., Qu, P., Yong, C., Wang, B., Feng, Y., Huang, H., Yang, L., and Hunter, C. (2022). Formable porous biochar loaded with La-Fe (hydr) oxides/montmorillonite for efficient removal of phosphorus in wastewater: process and mechanisms. Biochar *4*, 53. https://doi.org/10.1007/s42773-022-00177-8.

52. Tran, T.-T., Tran, N.-N.T., Sugiyama, S., and Liu, J.-C. (2021). Enhanced phosphate removal by thermally pretreated waste oyster shells. J. Mater. Cycles Waste Manag. *23*, 177–185.

53. Paradelo, R., Conde-Cid, M., Cutillas-Barreiro, L., Arias-Estévez, M., Nóvoa-Muñoz, J., Álvarez-Rodríguez, E., Fernández-Sanjurjo, M., and Núñez-Delgado, A. (2016). Phosphorus removal from wastewater using mussel shell: Investigation on retention mechanisms. Ecol. Eng. *97*, 558–566. https://doi.org/10.1016/j.ecoleng.2016.10.066.

54. Abdullah, N.H., Adnan, N.A., Mohd Rashidi, N.F.N., Yaacob, M.S.S., and Abdul Salim, N.A. (2022). Comparing the adsorption isotherms and kinetics of phosphate adsorption on various waste shells as adsorbent. Water Pract. Technol. *17*, 974–985. https://doi.org/10.2166/wpt.2022.051s.

55. Lee, J.-I., Kang, J.-K., Oh, J.-S., Yoo, S.-C., Lee, C.-G., Jho, E.H., and Park, S.-J. (2021). New insight to the use of oyster shell for removing phosphorus from aqueous solutions and fertilizing rice growth. J. Clean. Prod. *328*, 129536. https://doi.org/10.1016/j.jclepro.2021.129536.

STAR★METHODS

KEY RESOURCES TABLE

REAGENT or RESOURCE	SOURCE	IDENTIFIER
Chemicals, peptides, and recombinant proteins		
Potassium dihydrogen phosphate (KH_2PO_4)	Sinopharm Chemical Reagent Co., Ltd.	CAS: 7778-77-0
Lanthanum (III) chloride hexahydrate ($LaCl_3 \cdot 6H_2O$)	Sinopharm Chemical Reagent Co., Ltd.	CAS: 17272-45-6
Hydrochloric acid solution (HCl)	Sinopharm Chemical Reagent Co., Ltd.	CAS: 7647-01-0
Sodium hydroxide (NaOH)	Sinopharm Chemical Reagent Co., Ltd.	CAS: 1310-73-2
Iron (III) chloride hexahydrate ($FeCl_3 \cdot 6H_2O$)	Sinopharm Chemical Reagent Co., Ltd.	CAS: 10025-77-1
Iron (II) sulfate heptahydrate ($FeSO_4 \cdot 7H_2O$)	Sinopharm Chemical Reagent Co., Ltd.	CAS: 7782-63-0
Ammonium chloride (NH_4Cl)	Sinopharm Chemical Reagent Co., Ltd.	CAS: 12125-02-9
Sodium chloride (NaCl)	Sinopharm Chemical Reagent Co., Ltd.	CAS: 7647-14-5
Sodium Sulfate (Na_2SO_4)	Sinopharm Chemical Reagent Co., Ltd.	CAS: 7757-82-6
Magnesium chloride ($MgCl_2$)	Sinopharm Chemical Reagent Co., Ltd.	CAS: 7786-30-3
Humic acid	Sinopharm Chemical Reagent Co., Ltd.	CAS: 1415-93-6
N-2-hydroxyethylpiperazine-N′-2-ethanesulfonic acid	Sinopharm Chemical Reagent Co., Ltd.	CAS: 7365-45-9
Software and algorithms		
Orgin	OriginLab	https://www.originlab.com/

METHOD DETAILS

Raw materials

Clams were sourced from the breeding base in Haitou Town, Ganyu District, Lianyungang City, China, the largest clam breeding base in the region. The clam meat was extracted, and the remaining shells were meticulously washed with deionized water and air-dried for three days. Subsequently, the shells were crushed using a jaw crusher (OLAD-PSJ-100 × 60) and ground with a ball mill (YXQM-0.4L). They were then sieved through a nylon mesh (150 mesh) to obtain the final CS powder.

Material properties

The surface morphology and elemental composition were explored employing a Scanning electron microscope (SEM, FEI QUANTA 250G, USA) with integrated an Energy-dispersive X-ray spectrometer (EDS). A Brunauer-Emmet-Teller (BET) analyzer (JW-BK200, JWGB, Germany) was employed to evaluate the specific surface area (SSA) and pore size distribution (PSD). Magnetic features were explored through a vibrating sample magnetometer (VSM, MPMS-XL-7, Quantum Design, USA), while an X-ray diffraction (XRD) (Bruker, D8 ADVANCE, Germany) was utilized to identify the mineral composition. Chemical bond structures were analyzed using a Fourier transform infrared (FTIR) spectroscopy (Bruker, Tensor 27, Germany). Furthermore, electron binding energies were measured with an X-ray photoelectron spectroscopy (XPS, AXIS SUPRA+, Kratos, UK).

CS powder pretreatment

Previous studies indicate that calcination significantly enhances the pore structure of CS, facilitating the impregnation of active sites.[13] CS powder was calcined at 800°C for 2 h in a nitrogen atmosphere using a muffle furnace, resulting in calcined CS (CCS) powder. This calcination condition is commonly employed in bivalve shell modification studies. Typically, small amounts of impurities (e.g., organic matter) remain in the shells of bivalve shellfish, gradually decomposing when the calcination temperature exceeds 500°C.[52] Upon reaching 800°C, a sufficient reaction time of 2 hours ensures the effective removal of impurities.[53] Additionally, shell adsorbents produced under these conditions often exhibit the highest adsorption capacity.[54,55]

Preparation of La@Fe-CCS and Fe-CCS

Fe-CCS was processed through a modified co-precipitation technique,[25] as shown in Figure S1. First, 10 g of CCS was added to 250 mL of $FeCl_3 \cdot 6H_2O$ (0.1 mol/L) and 250 mL of $FeSO_4 \cdot 7H_2O$ (0.2 mol/L) solutions, and shaken in a water-bath oscillator at 200 rpm and 25°C for 30 minutes. The suspension was then heated to 70°C while being stirred, and pH was set to 10 by adding 2 mol/L NaOH. After oscillating for 0.3 hours, the product was magnetically separated, rinsed, dried, and milled to obtain Fe-CCS.

The preparation of La@Fe-CCS was carried out in two steps. First, a suspension containing Fe-CCS, as described above, was prepared. Then, 5 g of $LaCl_3 \cdot 6H_2O$ solution was added to the suspension, and the pH was adjusted to 10 using 2 mol/L NaOH. The mixture was oscillated for 0.3 hours. Finally, La@Fe-CCS was obtained using the same collection method as described above.

Adsorption tests

In these experiments, 250 mL conical flasks were used, and a measured quantity of adsorbent was added to each flask containing phosphate solution. The flasks were then placed on a shaking bed for 24 hours at 150 r/min and 25°C. Phosphate concentrations were measured at the end of the reaction. In all experimental batches, except for the pH effect tests and the treatment of actual domestic sewage, an appropriate concentration of N-2-hydroxyethylpiperazine-N'-2-ethanesulfonic acid (HEPES) buffer solution to stabilize the pH of the solution. This buffer solution is not prone to forming complexes with metals, making it a common choice for pH stabilization in adsorption experiments.[12] All experiments were conducted in triplicate, and the mean values of the results along with their associated error bars were reported. The adsorption equilibrium capacity (Q_e, mg/g) and removal rate (R, %) were determined through the expressions below:

$$Q_e = [(C_0 - C_e)/m] \times V \qquad \text{(Equation 15)}$$

$$R = [(C_0 - C_e)/C_0] \times 100\% \qquad \text{(Equation 16)}$$

Where C_O and C_e are the initial and equilibrium phosphate concentrations, mg/g; m is the adsorbent mass, g; and V is the solution volume, L.

The kinetics were assessed at different temperatures (288 K, 298 K, and 308 K). An adsorbent concentration of 1.5 g/L was added to 50 mL of phosphate solution (initial concentration of 10 mg/L), and samples were taken at fixed intervals (Fe-CCS: 10-1440 min; La@Fe-CCS: 5-120 min) to determine the phosphate concentration in the solution. The adsorption of phosphate by the adsorbents was analyzed using the pseudo-first-order (Equation 17) and pseudo-second-order (Equation 18) kinetic models because of their effectiveness in characterizing the kinetics of the adsorption process. Their adaptability enables broader application and facilitates comparisons with findings from other research.

$$In(Q_e - Q_t) = InQ_e - k_1 t \qquad \text{(Equation 17)}$$

$$t/Q_t = 1/k_2 Q_e + t/Q_e \qquad \text{(Equation 18)}$$

Where Q_t (mg/g) denotes the adsorbed amount at any moment t (min). k_1 (1/min) and k_2 (g/(mg·min)) are the pseudo-first-order and pseudo second-order rate constants, respectively.

The adsorption isotherms were fitted using the Langmuir (Equation 19) and Freundlich (Equation 20) models. Adsorption isotherm experiments were conducted by adding Fe-CCS and La@Fe-CCS to phosphate solutions with varying concentrations (5-60 mg/L, 5-100 mg/L), respectively. The R_L (separation factor) was calculated from the Langmuir constant, as presented in (Equation 21), to predict the ease of adsorption. When $R_L > 1$, adsorption is difficult; when $R_L = 1$, the process is linear; when $0 < R_L < 1$, adsorption is favorable; and when $R_L = 0$, adsorption is irreversible.

$$Q_e = Q_m K_L C_e / (1 + K_L C_e) \qquad \text{(Equation 19)}$$

$$Q_e = K_F C_e^{1/n} \qquad \text{(Equation 20)}$$

$$R_L = 1/(1 + K_L C_i) \qquad \text{(Equation 21)}$$

Where Q_m (mg/g) is the maximum adsorption capacity, K_L is the Langmuir constant, and K_F and $1/n$ are Freundlich constants. C_i is the initial concentration of phosphate (Fe-CCS: 60 mg/L; La@Fe-CCS: 100 mg/L).

The effect of temperature (288 K, 298 K, and 308 K) on the adsorption capacity of the adsorbent was analyzed. The solid-liquid partition coefficient (K_D), Gibbs free energy (ΔG^O, kJ/mol), enthalpy change (ΔH^0, kJ/mol), and entropy change (ΔS^O, J/(mol·K)) were calculated using (Equations 22, 23, and 24). R represents the ideal gas constant (8.314 J/(mol·K)), and T denotes the thermodynamic temperature in Kelvin (K).

$$K_D = \frac{Q_e}{C_e} \qquad \text{(Equation 22)}$$

$$\Delta G^0 = -RTIn(K_D) \qquad \text{(Equation 23)}$$

$$In(K_D) = -\frac{\Delta H^0}{RT} + \frac{\Delta S^0}{R} \qquad \text{(Equation 24)}$$

We also tested the effect of initial pH (2-11) on the removal of phosphate (initial concentration of 50 mg/L) by the adsorbent. The pH was adjusted using HCl and NaOH solutions (0.1 mol/L or 1 mol/L). Several common ions (SO_4^{2-}, CO_3^{2-}, Cl^-, NO^{3-}, Ca^{2+}, and Mg^{2+}) and Humic acid (HA) were selected to evaluate the adsorbent's ability to resist interference. The concentrations of the interfering ions were set at 10 mg/L, 50 mg/L, and 100 mg/L. The concentrations of HA were 5 mg/L, 15 mg/L, and 25 mg/L. The initial concentration of the phosphate solution was 20 mg/L.

Cyclic regeneration and practical application

The cyclic regeneration of La@Fe-CCS was tested over five cycles using 75 mg of La@Fe-CCS and 50 mL of 50 mg/L phosphate solutions. After each cycle, the adsorbent was desorbed using 1 mol/L NaOH, rinsed with deionized water, and then dried and ground at 105°C for reuse in subsequent cycles.

To verify the feasibility of La@Fe-CCS in practical sewage applications, this study focused on the effect of the adsorbent on the solidification of TP in real domestic sewage, using sewage from the family area of Jiangsu Ocean University as a sample. 150 mg of La@Fe-CCS was added to a container with 100 mL of domestic sewage and placed in an oscillator for reaction. Finally, the sample was passed through a 0.45 μm filter membrane for subsequent water quality analysis.

QUANTIFICATION AND STATISTICAL ANALYSIS

All statistical analyses and software used in this section are primarily Origin. Information about statistics have been given in the figure titles of Figures 3, 4, 5, 6, and 10.